



# The enhanced co-catalyst free photocatalytic hydrogen evolution and stability based on indenofluorene-containing donor-acceptor conjugated polymer dots/g-C<sub>3</sub>N<sub>4</sub> nanosheets heterojunction



Wei Zhou<sup>a,1</sup>, Tao Jia<sup>b,1</sup>, Dongqiao Zhang<sup>c</sup>, Zhikun Zheng<sup>a</sup>, Wei Hong<sup>a,\*</sup>, Xudong Chen<sup>a,\*</sup>

<sup>a</sup> Key Laboratory for Polymeric Composite and Functional Materials of Ministry of Education, School of Chemistry, Sun Yat-sen University, Guangzhou 510275, PR China

<sup>b</sup> Institute of Polymer Optoelectronic Materials and Devices, State Key Laboratory of Luminescent Materials and Devices, South China University of Technology, Guangzhou 510640, PR China

<sup>c</sup> School of Chemistry and Chemical Engineering, South China University of Technology, Wushan Road 381, Guangzhou, 510640, PR China

## ARTICLE INFO

### Keywords:

Poly(indenofluorene) dots  
Graphitic carbon nitride  
Photocatalytic hydrogen evolution  
Photocatalytic stability

## ABSTRACT

Due to the longer conjugation length and higher rigidity of the indenofluorene, poly(indenofluorene) (PIF) demonstrates better optical absorption capability and faster carriers mobility than the corresponding polyfluorene (PF). In this study, a donor-acceptor (D-A) type PIF (PIFDTBT) is synthesized and coupled with g-C<sub>3</sub>N<sub>4</sub> nanosheets to construct conjugated polymer dots/g-C<sub>3</sub>N<sub>4</sub> nanosheets (Pdots/CNNS). Ascribed to the enhanced light absorption, suitable band positions, and outstanding carriers mobility resulted by the introduction of indenofluorene units, the HER of PIFDTBT Pdot/CNNS is 7.6 times higher than that of F8DTBT Pdots/CNNS at the 1<sup>st</sup> run without metallic co-catalyst. Interestingly, the HER enhancement of PIFDTBT Pdots/CNNS compared to F8DTBT Pdots/CNNS correspondingly increases from 7.6 times at the 1<sup>st</sup> run to 14.3 times at the 4<sup>th</sup> run. This research can provide an insight for constructing organic nanocomposites with improved optical response and enhanced stability by electron donor units adjustment of the conjugated polymer.

## 1. Introduction

The water-splitting photocatalysis is regarded as a green and sustainable approach to resolve energy crisis resulted from superfluous consumption of fossil fuels [1–3]. In the various artificial photocatalysts developed, graphitic carbon nitride (g-C<sub>3</sub>N<sub>4</sub>) demonstrates excellent prospects ascribed to its facile preparation, metal-free structure, photocorrosion resistance, thermal and chemical stability [4–14]. However, the bulk g-C<sub>3</sub>N<sub>4</sub> has several disadvantages that lead to unsatisfactory photocatalytic performance, such as relatively low specific surface area, insufficient active sites, fast photo-induced carriers recombination, and limited visible light absorption range resulting in an inadequate visible light harvesting [15,16].

To improve photocatalytic performance, various modified g-C<sub>3</sub>N<sub>4</sub> has been developed, including nanoengineering (nanodots [17], nanorods [18,19], nanowires [20,21], nanosheets [22,23], porous structures [24,25]), chemical dopings (B [26,27], P [28,29], F [30], S [31,32]) and heterojunction constructions (metallic nanoparticle/g-C<sub>3</sub>N<sub>4</sub> [33,34], metallic compound nanoparticle/g-C<sub>3</sub>N<sub>4</sub> [35–37],

carbon-based g-C<sub>3</sub>N<sub>4</sub> [15,38–40], and isotype g-C<sub>3</sub>N<sub>4</sub>/g-C<sub>3</sub>N<sub>4</sub> [41]). However, all of the above modifications possess respective deficiencies: introduction of poisonous noble metals as co-catalysts for almost all of the above modifications; narrow extent for visible light absorption for nanoengineering, chemical dopings, and metal-containing heterojunctions; limited approaches of bandgap adjustments, low efficiency of photo-induced charge-hole pairs separation and transfer for carbon-based g-C<sub>3</sub>N<sub>4</sub> heterojunctions. Therefore, an idealistic modified g-C<sub>3</sub>N<sub>4</sub> photocatalyst should have excellent light absorption capability, multiple active sites, efficient carriers separation and transfer, diverse bandgap adjustments, and co-catalysts free properties. To resolve the above mentioned issues for photocatalysis, the metal-free conjugated polymer/g-C<sub>3</sub>N<sub>4</sub> composites, with excellent light absorption and various approaches of bandgap adjustments, have been regarded as a new method for photocatalysis [42–45]. A conjugated polymer applied to construct conjugated polymer/g-C<sub>3</sub>N<sub>4</sub> heterojunction should take two crucial aspects into accounts: 1. broad absorption range, high absorption coefficient, suitable bandgap and fast carriers mobility. 2. high photocatalytic stability under light irradiation [46–49].

\* Corresponding authors.

E-mail addresses: [hongwei9@mail.sysu.edu.cn](mailto:hongwei9@mail.sysu.edu.cn) (W. Hong), [cescxd@mail.sysu.edu.cn](mailto:cescxd@mail.sysu.edu.cn) (X. Chen).

<sup>1</sup> Wei Zhou and Tao Jia contributed equally to this work.

The construction of donor-acceptor (D–A) structure with alternating repeating units has been regarded as an effective strategy to obtain conjugated polymer of suitable bandgap and high absorption efficiency. Different from the donor-donor (D–D) structure, the DA–structure can generate intramolecular charge transfer (ICT) from donor to acceptor segments, thus effectively extending the visible light absorption and adjusting energy levels [44,50,51]. Presently, the poly-fluorene family polymers (PFs) with D–A structures, such as poly(9,9-di-octylfluorene-alt-benzothiadiazole) (F8BT) [52], poly(N-decanyl-2,7-carbazole-alt-9,9-di-octylfluorene) (PCzF) [52] and poly(9,9-di-octyl-fluorene-alt-bithiophene) (F8T2) [53] etc, have been employed to couple with g-C<sub>3</sub>N<sub>4</sub> to construct PF/g-C<sub>3</sub>N<sub>4</sub> heterojunctions which can improve the photocatalytic hydrogen evolution rate (HER) due to the suitable bandgap and good visible light absorption efficiency. It should be noted, up to now, to adjust the light absorption range and bandgap, the D–A type PFs applied to photoacatalysis mainly focus on the alteration of electron acceptor, such as benzothiadiazole, carbazole or bithiophene. While, in fact, the light harvesting band and carriers mobility of PFs can be also improved by altering rigid electron donor structure of the backbone, which has been proved to be beneficial for optical devices [54]. Therefore, it can be expected that PIFs adopted to combine with g-C<sub>3</sub>N<sub>4</sub> can further improve HER performance. To adjust the rigid electron donor structure of the PF backbone, a well-known effective strategy is an introduction of the indenofluorene (IF) units to replace the fluorene units. The structure of indenofluorene can be considered as the linear overlap of two fluorene units. Significantly, the PIF demonstrates more intense absorption band and faster carriers mobility than those of PF due to its longer effective conjugation length and higher planarity [54,55]. In addition, in an indenofluorene-containing conjugated polymer, four long alkyl chains are introduced to every unit of the backbone, which can provide an improved solution processability for PIF compared with that of PF [55]. Therefore, the indenofluorene has been considered as a very important building monomer to construct functional conjugated polymers, which have been widely applied in various optoelectronic devices. Reasonably, the PIF consisted of indenofluorene units and electron acceptor units can be also applied to couple with g-C<sub>3</sub>N<sub>4</sub> for photocatalysis.

Another crucial issue is the photocatalysis stability which is largely determined by the stability of the photocatalyst. In a g-C<sub>3</sub>N<sub>4</sub> nanosheets photocatalysis system, it has been revealed that organic dyes can be oxidized by O<sub>2</sub><sup>•-</sup> and OH<sup>•</sup> generated by g-C<sub>3</sub>N<sub>4</sub> nanosheets under light irradiation and air conditions [56]. Intriguingly, it has been reported, in donor-donor (D–D) type pyrene-based polymer (PyP<sub>2</sub>)/bulk g-C<sub>3</sub>N<sub>4</sub> heterojunction, PyP<sub>2</sub> demonstrates excellent photo-corrosion capability without structural destroy which can be due to the rigid structure with excellent resistance to radial groups [57]. As a comparison, it has been found that the D–A type PF/g-C<sub>3</sub>N<sub>4</sub> photocatalyst with TEOA as radical scavenger shows significant PF decomposition owing to the generation of radical groups during photocatalysis, leading to obvious HER decrease under light irradiation [53]. Therefore, it can be seen, due to the stronger rigidity of D–D structure than DA– structure, pyrene-based polymer has an improved photo-corrosion resistance than that of D–A type PF. As the improved rigidity of PIF, it can be further speculated that a PIF/g-C<sub>3</sub>N<sub>4</sub> possesses better photocatalytic stability than that of PF/g-C<sub>3</sub>N<sub>4</sub>. Moreover, a reasonable adjustment of radical scavenger addition during photocatalysis can be also possible to further promote the capture for oxygen-containing radicals under light irradiation, thus enhancing the photocatalysis stability.

In this study, a poly(indenofluorene) with excellent optical absorption and fast hole carriers mobility was synthesized by the copolymerization of indenofluorene units with benzothiadiazole units (PIFDTBT) (Fig. 1A), and coupled with porous g-C<sub>3</sub>N<sub>4</sub> nanosheets (CNNS) of high surface area through a facile solution method to form PIFDTBT polymer dots/g-C<sub>3</sub>N<sub>4</sub> nanosheets (PIFDTBT Pdots/CNNS) to increase the photocatalysis reaction sites, improve the electron-hole pair separation and transfer and enhance the interfacial interaction

(Fig. 1B). Owing to the better light absorption capability, more suitable energy level difference and faster carriers mobility, PIFDTBT Pdots/CNNS showed outstandingly higher HER than that of F8DTBT Pdots/CNNS heterojunction without any co-catalysts. Moreover, PIFDTBT Pdots/CNNS also had improved photocatalysis stability compared to F8DTBT Pdots/CNNS. Significantly, a re-addition of TEOA radical scavenger could obviously improve the HER stability of PIFDTBT Pdots/CNNS. This research can broaden a horizon for conjugated polymer-based nanocomposite, possessing excellent light harvesting, fast carriers mobility, metal-free composition and enhanced stability, in the applications of photocatalysis and optical devices.

## 2. Experimental

### 2.1. Chemicals

Poly((2,7-(9,9-(di-n-octyl)fluorene)-alt-5,5-(4',7'-di-thienyl-2',1',3'-benzothiadiazole)) (F8DTBT, Mn = 13.1 kDa, PDI = 1.86) was purchased from Derthon Optoelectronic Materials Science Technology Co., Ltd. Pd(PPh<sub>3</sub>)<sub>4</sub>, K<sub>2</sub>CO<sub>3</sub>, A336 and urea were supplied by Aladin Co., Ltd. 5,5'-dimethyl-1-pirroline-Noxide (DMPO) was purchased from Macklin Chemical Co., Ltd. All chemicals and reagents with analytical grade were used without further purification.

### 2.2. Synthesis of poly(indenofluorene) (PIF)

2,2'-(6,6,12,12-Tetraocty-6,12-dihydroindeno[1,2b]fluorene-2,8-diyl) bis(4,4,5,5-tetramethyl-1,3,2-dioxaborolane) (IFB) [55] and 4,7-di(2-bromothien-5-yl)-2,1,3-benzothiadiazole (DBrTBT) [58,59] were respectively synthesized according to previously published references. As shown in Fig. 1A, PIFDTBT was synthesized as follows: The purified IFB (191 mg, 0.2 mmol), DBrTBT (179.2 mg, 0.2 mmol), A336 (0.04 ml) and aqueous K<sub>2</sub>CO<sub>3</sub> solution (1 ml, 2 M) were sequentially added into a 25 mL two-neck flask containing toluene (3 ml). After the flask was degassed for 0.5 h with argon gas, Pd(PPh<sub>3</sub>)<sub>4</sub> (3.6 mg) was added to the mixture above, then the degassed reaction mixture was allowed to stir for 24 h in a refluxed condition under an argon atmosphere. Subsequently, the solution was poured into methanol, then the crude precipitate was successively extracted with methanol, dichloromethane, and chloroform by Soxhlet extraction. The co-polymer solution in chloroform was evaporated to 10 ml, and then the condensed solution was slowly poured into 500 mL methanol. The purified product was collected and dried under vacuum (yield = 82 wt%, Mn = 14.6 kDa, PDI = 1.63). The <sup>1</sup>H NMR data of PIFDTBT (Fig.S1A, 300 MHz, CDCl<sub>3</sub>) is as follows: 8.18 (m, 2 H), 7.97 (m, 2 H), 7.81–7.76 (m, 4 H), 7.70–7.66 (m, 4 H), 7.54 (m, 2 H), 2.10–2.01 (m, 8 H), 1.20–1.10 (m, 48 H), 0.80–0.77 (m, 12 H). The FT-IR peaks of characteristic groups in PIFDTBT (Fig.S1B) is as follows: 3037–2847, 1490–1428 and 1373–1334 cm<sup>-1</sup>.

### 2.3. Preparation of g-C<sub>3</sub>N<sub>4</sub> nanosheets

The g-C<sub>3</sub>N<sub>4</sub> nanosheets were prepared based on a previous publication [22]. First, the bulk g-C<sub>3</sub>N<sub>4</sub> sheets (CNS) were prepared with urea as the precursor through thermal polymerization. Typically, 10 g urea was polymerized in a muffle furnace under air atmosphere at 550 °C (heating rate: 5 °C/min) for 2 h to obtain CNS. Subsequently, 0.5 g bulk CNS powder was thermally treated by heating at 500 °C under an Ar-carrying water atmosphere (heating rate: 5 °C/min) for 4 h to obtain g-C<sub>3</sub>N<sub>4</sub> nanosheets (CNNS).

### 2.4. Fabrication of Pdots/CNNS heterojunctions

F8DTBT and PIFDTBT were respectively dispersed on the surface of CNNS in chloroform. Typically, 60 mg CNNS and 3 mg PIFDTBT were respectively added to 30 mL chloroform in a round-bottom flask, and

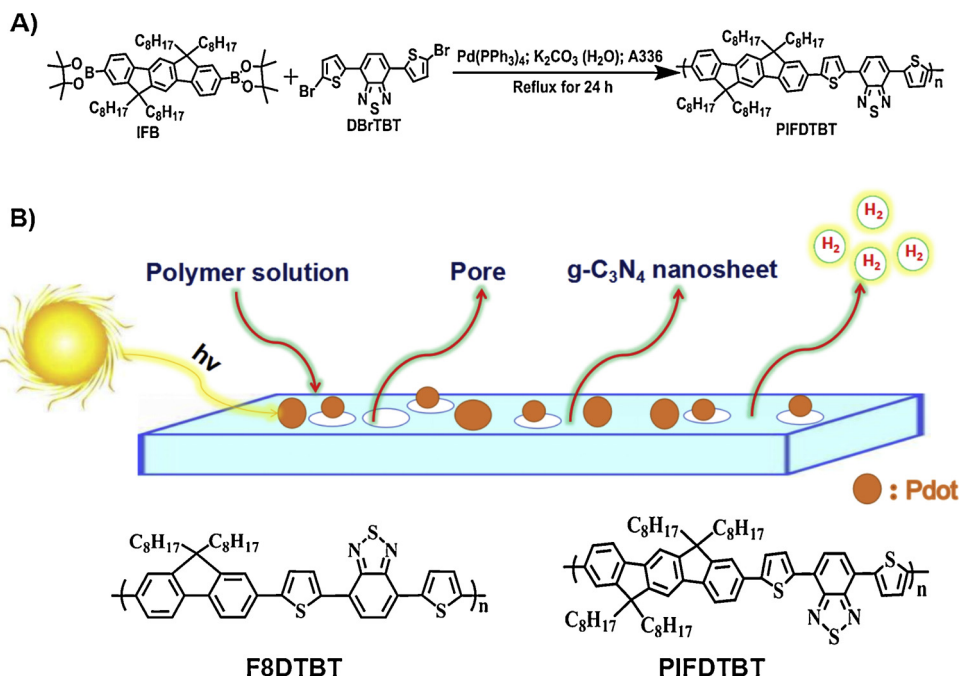


Fig. 1. A)The synthesis route of PIFDTBT. B)The fabrication of Pdots/g-C<sub>3</sub>N<sub>4</sub> nanosheets heterojunction.

the mixture was maintained stirring at room temperature for 24 h. Finally, PIFDTBT Pdots/CNNS heterojunction-5% was obtained by vacuum evaporation at 30 °C. Similarly, PIFDTBT Pdots/CNNS heterojunctions with a certain weight ratio of PIFDTBT to CNNS (1, 3, 7 wt%), F8DTBT Pdots/CNNS-5% and PIFDTBT/CNS-5% were fabricated based on the method above, respectively.

### 2.5. Device fabrication for carriers mobility tests

The devices for carriers mobility tests were fabricated with a ITO/PEDOT: PSS/Active layer/mMoO<sub>3</sub>/Ag structure in a glove box. The glass substrate covered by indium tin oxide (ITO, 15 Ω sq.<sup>-1</sup>) was respectively cleaned by detergent, water, acetone, and isopropyl alcohol for 20 min under ultrasonic condition. Then the ITO substrate was treated by plasma for 4 min after being dried in an oven at 80 °C overnight. A thin poly(3, 4-ethylenedioxythiophene)/poly(styrene sulfonic acid) (PEDOT: PSS) layer (filtered through a 0.45 μm PES filter, ~40 nm) was spin-coated onto the substrate, which was baked for 15 min at 150 °C under air condition. Successively, the PIFDTBT or F8DTBT was spin-coated onto the ITO/PEDOT:PSS substrate. Finally, the cathode, a bilayer of a thin MoO<sub>3</sub> layer (10 nm) covered with Ag (80 nm), was thermally evaporated through a shadow mask onto the prepared interlayer in a vacuum chamber with the pressure of 2 × 10<sup>-7</sup> mbar.

### 2.6. Characterization

The <sup>1</sup>H nuclear magnetic resonance (<sup>1</sup>H NMR) were carried out with a 600 MHz nuclear magnetic resonance instrument (AVANCE III HD 600, Bruker). The Fourier Transform infrared (FT-IR) spectra were collected by a FT-IR spectrometer (NICOLET 6700). The gel permeation chromatography (GPC) test was carried out at room temperature utilizing tetrahydrafuran (THF) as an eluent (flow rate: 1.0 mL/min) on a Waters GPC system. The nitrogen adsorption-desorption isotherms curves were collected by a Micromeritics (ASAP 2040, Micrometrics Inc.) at 77 K with all samples degassed at 398 K for 10 h prior to measurements. The UV-vis diffuse reflectance spectra (DRS) were obtained (BaSO<sub>4</sub> powder as the reference) by a spectrophotometer (Shimadzu UV-3600). The Photoluminescence (PL) spectra (wavelength range:

400–800 nm) were measured at room temperature with excitation wavelength of 340 nm by a fluorescence spectrometer (Edinburgh FLS 920). The electron paramagnetic resonance (EPR) spectra were conducted with a Bruker A300 spectrometer under dark or light irradiation condition. The electron spin resonance (ESR) signals of superoxide radical were spin-trapped by DMPO in methanol under visible-light irradiation. The X-ray diffraction (XRD) tests were performed by an X-ray diffractometer (D8 Advance Bruker) with CuKα ( $\lambda = 1.5406 \text{ \AA}$ ) irradiation source at 40 kV. The transmission electron microscopy (TEM) images and the STEM elemental distributions images were acquired on a field-emission microscope (JEOL JEM-2100F). The X-ray photoelectron spectrometry (XPS) and XPS valence spectra tests were conducted on a XPS instrument (Thermo ESCALab250) with the binding energies calibrated by C 1s peak at 284.8 eV. The cyclic voltammetry (CV) measurements were conducted on a electrochemical workstation (CHI600D) utilizing a standard three-electrode cell with a reference electrode (saturated calomel electrode, SCE), a counter electrode (platinum electrode), and a work electrode (ITO glass coated by PIFDTBT or F8DTBT). The testing potential ranged from -2.5 to 2.5 V with the scanning rate of 0.05 V/s with the electrolyte solution of 0.1 M tetrabutylammonium hexafluorophosphate (NBu<sub>4</sub>PF<sub>6</sub>)/acetonitrile. The obtained CV potentials were recorded against ferrocene/ferrocenium (Fc/Fc<sup>+</sup>). Different from the CV testing, the Mott-Schottky plots of the g-C<sub>3</sub>N<sub>4</sub> were performed by three electrodes with a Pt plate, an Ag/AgCl and a ITO substrate coated by g-C<sub>3</sub>N<sub>4</sub>. The bias voltage ranged from -0.45 to 0.85 V at three different frequencies of 1000, 1800 and 2700 Hz with 0.1 M Na<sub>2</sub>SO<sub>4</sub> aqueous solution as electrolyte. The electrochemical impedance spectroscopy (EIS) were conducted at the frequency range of 0.01–100 kHz in 0.1 M Na<sub>2</sub>SO<sub>4</sub> solution under the same conditions as Mott-Schottky plots measurements. Photocurrent measurements were carried out in 0.1 M Na<sub>2</sub>SO<sub>4</sub> solution with the same three-electrode system of EIS tests. The bias potential was 0.1 V with visible light generated by a 300 W xenon lamp ( $\lambda > 400 \text{ nm}$ ). The surface photovoltage (SPV) spectra were carried out with a surface photovoltage spectrometer (PL-SPV/IPCE1000, Beijing Perfectlight Inc., China) equipped with a monochromatic light source, a lock-in amplifier with a light chopper, and a sample cell. The elemental analysis were performed by a Vario EL Elemental Analyzer.

### 2.6.1. Carriers mobility measurement of device

The carriers mobility was determined by fitting the dark J-V current to a single-carrier SCLC model as follows.

$$J = (9/8)\varepsilon_0\varepsilon_r\mu((V^2)/(d^3)) \quad (1)$$

where  $J$ ,  $\varepsilon_0$ ,  $\varepsilon_r$ ,  $\mu$ ,  $d$  and  $V$  is the current, permittivity of free space, relative permittivity of the material, zero-field mobility, thickness of the single active layer and effective voltage, respectively. Through subtracting the built-in voltage ( $V_{bi}$ ) and the voltage drop ( $V_s$ ) from the substrate's series resistance from the applied voltage ( $V_{app}$ ), the effective voltage ( $V$ ) can be obtained,  $V = V_{app} - V_{bi} - V_s$ . The hole carriers mobility can be calculated from the slope of the  $J_{1/2}\sim V$  curve.

### 2.6.2. Photocatalytic HER tests

The photocatalytic HER of pure g-C<sub>3</sub>N<sub>4</sub>, conjugated polymers, and heterojunctions composites were conducted under visible light irradiation provided by a 300 W Xe lamp (Labsolar 6A, Beijing Perfectlight Inc., China) with a 400 nm cut-off filter. The light intensity was 3820 W·m<sup>-2</sup>. Typically, a mixture, 20 mg PIFDTBT Pdot/CNNS powder dispersed in 100 ml water with 10 vol % TEOA as radical scavenger, was added to a top-irradiation reaction vessel. The system was degassed prior to photocatalysis. The photocatalysis reaction was maintained for 5 h at room temperature. The H<sub>2</sub> evolution was analyzed by a gas chromatography (7900, Techcomp) with 5 Å molecular sieve columns by Ar as carrier gas.

The apparent quantum yield (AQY) for the H<sub>2</sub> production was calculated by the equation as follows:

$$AQY(\%) = \frac{2 \times M \times N_A \times h \times c}{S \times P \times t \times \lambda} \times 100\% \quad (2)$$

where  $M$  is the production of H<sub>2</sub> (mole per s),  $N_A$  is the Avogadro constant ( $6.02 \times 10^{23}/\text{mol}$ ),  $h$  is the Planck constant ( $6.62 \times 10^{-34} \text{ J}\cdot\text{s}$ ),  $c$  is the light speed under vacuum ( $3.0 \times 10^8 \text{ m}\cdot\text{s}^{-1}$ ),  $S$  is the area of light irradiation ( $11.02 \times 10^{-4} \text{ m}^2$ ),  $\lambda$  is the light wavelength (420, 450, 475, 500, 520, 550 and 600 nm, respectively),  $P$  is the incident monochromatic light intensity (5.02, 56.0, 87.8, 90.5, 196.0, 125.9, 99.1 W·m<sup>-2</sup> for 420, 450, 475, 500, 520, 550 and 600 nm, respectively),  $t$  is the irradiation time at different wavelength (3600 s).

## 3. Results and discussion

### 3.1. Morphology of heterojunctions

Since the dispersion of conjugated polymer is significant for the optical, electrochemical properties and photocatalysis activity of the heterojunction, we presented a study of micro-morphology investigated by TEM. PIFDTBT Pdots/CNNS and F8DTBT Pdots/CNNS were respectively dispersed in water under ultrasonic condition, then dropped onto copper membrane and characterized by TEM. The TEM images indicated the confined Pdots were stable and uniformly-dispersed on the porous CNNS and did not get detached even under ultrasonic vibration due to the bilateral interaction between Pdots and CNNS (Fig. 1A). The HRTEM images for PIFDTBT Pdots/CNNS (Fig. 2A) and F8DTBT Pdots/CNNS (Fig.S2A) clearly showed the micro-morphology of Pdots on the surface as confirmed by the STEM images for the sulfur (S) distribution was almost consistent with the Pdots distribution, which was further identified that the Pdots were consisted of conjugated polymer (Fig. 2B-E, Fig.S2B-E). Furthermore, it could be clearly observed that some relatively large PIFDTBT Pdots with an average diameter of 9.1 nm were dispersed on CNNS. It should be also noted that there were PIFDTBT Pdots with the diameter less than 1 nm uniformly distributed on the surface (Fig. 2A). Additionally, F8DTBT Pdots were also well-distributed on CNNS surface with an average diameter of 8.5 nm (Fig.S2A). To further confirm the positive influence of CNNS for the formation of Pdots, PIFDTBT was adopted to couple with bulk g-C<sub>3</sub>N<sub>4</sub> (CNS). As a comparison, it could be proved by TEM

image that PIFDTBT was poorly dispersed on the surface of bulk CNS (Fig.S3).

The active centers are closely related to the specific surface area of Pdots heterojunctions. Therefore, the specific surface area and pore distribution of CNNS and Pdots/CNNS were determined by nitrogen absorption-desorption isotherms with the Barrett-Joyner-Halenda (BJH) model (Fig. 2F-G). The significantly reduced surface area and average pore size for PIFDTBT Pdots/CNNS suggested that PIFDTBT Pdots were occupied in the mesopores of CNNS (Fig.S4, Table S1). Therefore, it could be suggested that the uniformly distributed PIFDTBT Pdots can be attributed to the structurally porous CNNS with the high surface area.

### 3.2. The hole carriers mobility of F8DTBT and PIFDTBT, band position and photophysical characteristics of Pdots/CNNS heterojunction

The carriers mobility has close relationship with the charge and hole transfer of the conjugated polymer. The current density versus voltage characteristics were detected to calculate the hole carriers mobility of the P-type F8DTBT and PIFDTBT (Fig.S4A). The film thickness of PIFDTBT and F8DTBT was 58 and 100 nm, respectively. By a calculation from the equation, the hole carriers mobility ( $\mu_h$ ) for PIFDTBT and F8DTBT was  $1.11 \times 10^{-3}$  and  $1.72 \times 10^{-4} \text{ cm}^2 \text{ V}^{-1} \text{ s}^{-1}$ , respectively. It could be seen that 6.45 times hole carriers mobility enhancement for PIFDTBT should be ascribed to the relatively long effective chains and high planarity compared to F8DTBT [54].

The light absorption range and efficiency have important influence on photocatalysis, therefore, UV-vis DRS was employed to observe the absorption intensity and edge of the heterojunctions. It is well-known that the visible light (400–700 nm) energy mainly dominates the whole sunlight energy distribution. To improve the absorption efficiency of sunlight, it is quite necessary to extend the visible light absorption range of a photocatalyst. It could be observed that the absorption edge for CNNS, F8DTBT and PIFDTBT were respectively located at 436, 663 and 671 nm in Fig. 3A. Notably, due to the relatively long effective conjugated chain of PIFDTBT, the optical absorption intensity was enhanced compared to those of F8DTBT (Fig. 3A), which was consistent with the previously published literature [54,58]. It should be also noted that PIFDTBT Pdots/CNNS and F8DTBT Pdots/CNNS showed red-shift with tail absorption compared to the pristine polymers (Fig. 3A), which could be owed to the  $\pi-\pi^*$  interaction between Pdots and CNNS, leading to reduced  $\pi-\pi^*$  transition energy [60,61]. And due to the better absorption capability of PIFDTBT, PIFDTBT Pdots/CNNS also showed higher light absorption intensity than that of F8DTBT Pdots/CNNS. Besides, the absorption intensity of PIFDTBT Pdots/CNNS heterojunction increased with an increased amount of PIFDTBT (Fig.S5). The band structure of the conjugated polymers and CNNS in the diagram (Fig. 3B) was determined by the tauc plots (Fig.S6), XPS valance spectra (Fig.S7), Mott-Schottky plots (Fig.S8) and cyclic voltammetry (CV) (Fig.S9). It could be seen that PIFDTBT, with electron-donating indenofluorene units, demonstrated more negative conduction band (CB) and less positive valence band (VB) than F8DTBT (Fig. 3B, Table S2). The energy level difference could drive the photogenerated electrons transfer from PIFDTBT to CNNS and the photoexcited hole carriers transfer from CNNS to PIFDTBT.

To further understand the crucial role of Pdots in accelerating photogenerated electrons transfer, the steady-state photoluminescence (PL) spectra of CNNS (dispersed in water), conjugated polymers (dispersed in CHCl<sub>3</sub>), and Pdots/CNNS (dispersed in water) were measured to detect the recombination of charge-hole pairs without co-catalysts under the excitation wavelength of 340 nm (Fig. 3C). It could be observed that CNNS, PIFDTBT and F8DTBT showed a strong emission peak centered at 435, 690 and 680 nm, respectively. Interestingly, after the combination of CNNS and PIFDTBT, the corresponding characteristic peak intensities for Pdots/CNNS were remarkably quenched, which was resulted from the fast excited charge-hole carriers transfer through an interfacial  $\pi-\pi$  interaction between PIFDTBT Pdots and CNNS,

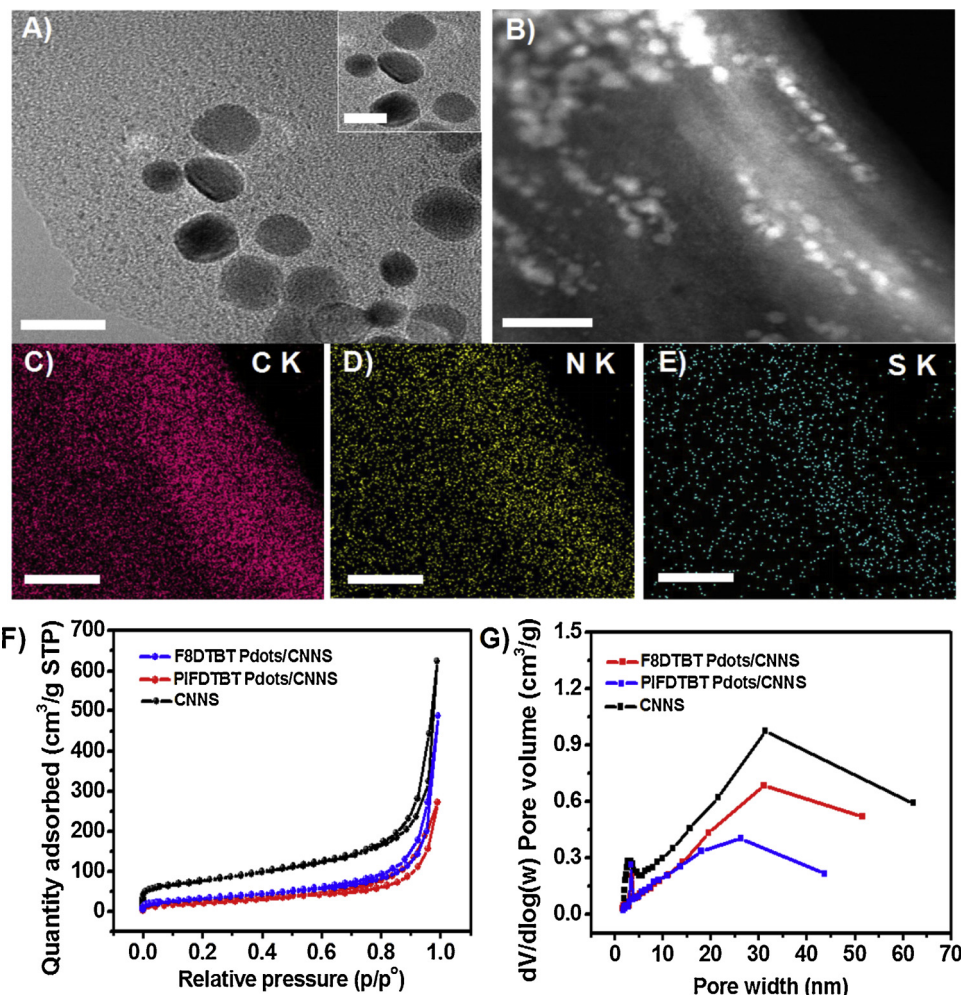


**Fig. 2.** TEM images of A) PIFDTBT Pdots/CNNS (scale bar: 20 nm, inset: HRTEM of PIFDTBT Pdots/CNNS, scale bar: 5 nm. STEM images of B) testing area of PIFDTBT Pdots/CNNS, C, D) N, and E) S distribution of PIFDTBT Pdots/CNNS (scale bars: 30 nm), respectively. F) The nitrogen adsorption-desorption isotherm curves of CNNS and Pdots/CNNS. G) The pore size distribution of CNNS and Pdots/CNNS. The Pdots to CNNS mass ratios were 5 wt%.

significantly inhibiting the direct recombination of photoexcited charges and holes. Particularly, it could be observed that PIFDTBT Pdots/CNNS heterojunction demonstrated much weaker PL intensity than that of the F8DTBT Pdots/CNNS at the excitation of 435 nm. A well-known reason for PL quench is the charge-hole pairs transfer due to the energy level difference of heterojunction [45]. The CB of CNNS and PIFDTBT was -1.00 and -1.10 V, respectively, and the VB of CNNS and PIFDTBT was 1.84 and 0.75 V, respectively (Fig. 3B), therefore the photogenerated electrons could transfer from the CB of PIFDTBT to that of CNNS and hole carriers could transfer from the CB of CNNS to that of PIFDTBT, which could promote PL intensity quench. However, probably due to the relatively insignificant energy level difference of F8DTBT Pdots/CNNS (Fig. 3B), the PL intensity of F8DTBT Pdots/CNNS was much less quenched than that of PIFDTBT Pdots/CNNS. Besides, the PL intensity of PIFDTBT Pdots showed a decreasing tendency with the increased mass ratio of PIFDTBT (Fig.S10A).

Time-resolved PL decay spectroscopy was employed to reveal the photogenerated electrons dynamics of Pdots/CNNS heterojunctions (Fig. 3D). The characteristic emissions of CNNS, PIFDTBT and F8DTBT followed decay with an average lifetime of 6.28, 2.90 and 3.61 ns (Table S3), respectively. The coupling of PIFDTBT with CNNS could significantly prolong the lifetime for PIFDTBT Pdots (680 nm) to 4.71 ns, while F8DTBT Pdots (690 nm) showed lifetime decrease to 2.09 ns (Table S3). It could be speculated that the prolonged lifetime of PIFDTBT Pdots could be owed to the energy level difference that

accelerated the carriers transfer through  $\pi$ - $\pi$  interaction, which inhibited the charge-hole pairs recombination for the heterojunction. While the decreased lifetime of F8DTBT Pdots could be due to increased hole carriers transfer from CNNS to F8DTBT and inefficient photo-generated electrons transfer from F8DTBT to CNNS, which leaded to fast charge-hole pairs recombination. However, in this work, the CNNS (450 nm) in all Pdots/CNNS demonstrated lifetime decrease. In general, it is believed that effective heterojunction could increase the PL lifetime of the semiconductor because of the increased separation and transfer efficiency. However, it was also common to see a decreased PL lifetime such as 0D/2D heterojunctions of vanadate quantum dots/graphitic carbon nitride nanosheets [62] and 2D/2D heterojunctions of SnS<sub>2</sub> nanosheets/graphitic carbon nitride nanosheets [63]. In these systems, the reduced lifetime was believed as a result of the non-radiative pathway from the electronic interaction between the two phases.

In this Pdots/CNNS heterojunction, there could be at least two factors leading to the reduced PL lifetime: the reduced surface area and the non-radiative pathway from the electronic interaction between CNNS and the conjugated polymer dots. On one hand, it is believed that the lifetime of g-C<sub>3</sub>N<sub>4</sub> is related the surface area because the high surface area of the g-C<sub>3</sub>N<sub>4</sub> means defects which can trap the excitons, leading to the increased lifetime of g-C<sub>3</sub>N<sub>4</sub> [14,22]. In this work, it was found that the Pdots/CNNS heterojunctions demonstrated reduced BJH surface areas when compared with CNNS, which could be ascribed to the pores occupation by Pdots (Table S1), thus leading to the lost

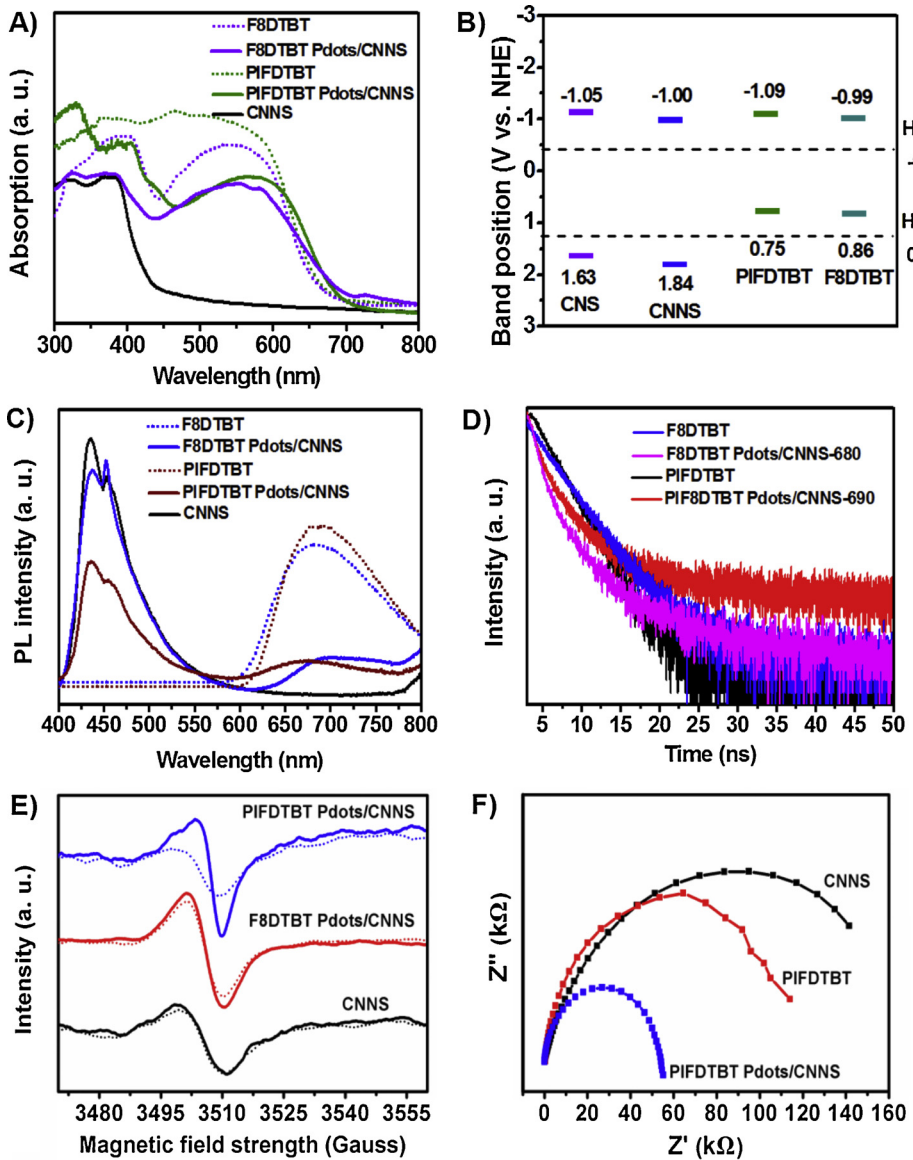


**Fig. 3.** A) UV-vis DRS of CNNS, F8DTBT, PIFDTBT and Pdots/CNNS. (The F8DTBT and PIFDTBT had the same weight for DRS tests, and the PIFDTBT Pdots/CNNS and F8DTBT Pdots/CNNS had the same weight for DRS tests); B) The band position diagram of  $\text{g-C}_3\text{N}_4$ , F8DTBT and PIFDTBT; C) PL spectra of CNNS, PIFDTBT, F8DTBT, PIFDTBT Pdots/CNNS and PIFDTBT Pdots/CNNS under excitation of 340 nm (CNNS, PIFDTBT Pdots/CNNS and PIFDTBT Pdots/CNNS were dispersed in water; PIFDTBT and F8DTBT were dissolved in  $\text{CHCl}_3$ ); D) Time-resolved PL spectra of PIFDTBT, F8DTBT, PIFDTBT Pdots/CNNS and PIFDTBT Pdots/CNNS monitored at 690, 680, 690 and 680 nm, respectively, under excitation of 340 nm at 298 K (CNNS, PIFDTBT Pdots/CNNS and PIFDTBT Pdots/CNNS were dispersed in water; PIFDTBT and F8DTBT were dissolved in  $\text{CHCl}_3$ ). E) EPR spectra of CNNS, F8DTBT Pdots/CNNS and PIFDTBT Pdots/CNNS under a dark or visible light condition (dash lines: in dark; solid lines:  $\lambda > 400 \text{ nm}$ ) at room temperature; F) EIS of PIFDTBT, CNNS and PIFDTBT Pdots/CNNS. The Pdots to CNNS mass ratios were 5 wt%.

capacity to trap excitons and decreased lifetime. On the other hand, the Pdots/CNNS heterojunctions could lead to the non-radiative pathway from the electronic interaction between them, which also led to the reduced lifetime.

To further confirm the correctness of lifetime change for CNNS, PIFDTBT, F8DTBT, PIFDTBT Pdots/CNNS and F8DTBT/CNNS, the lifetime tests of all solid samples without dispersed in solvents were carried out. As shown in (Fig.S11, Table S4), the lifetime of CNS (450 nm), CNNS (450 nm), PIFDTBT (680 nm) and F8DTBT(690 nm) was 2.58, 5.80, 0.17 and 0.95 ns, respectively. The lifetime of CNNS showed significant increase compared to that of CNS could be due to the obvious specific surface area increase. The PIFDTBT Pdots (680 nm) in PIFDTBT Pdots/CNNS increased from 0.17 to 0.43 ns, while F8DTBT Pdots (690 nm) in F8DTBT Pdots/CNNS decreased from 0.95 to 0.13 ns. Simultaneously, the CNNS (450 nm) in all Pdots/CNNS also demonstrated lifetime decrease. It could be seen that the regularity of lifetime change of all Pdots in Pdots/CNNS was consistent with those tested in water condition. Therefore, it could be concluded that the decreased lifetime of CNNS in Pdots/CNNS could be owed to the decreased specific area of Pdots/CNNS.

With regards to structure adjustment of donor units for PIF, the charge carrier separation and transfer within heterojunctions were

investigated by EPR in the magnetic field from 3470 to 3560 G with the same sample weight (Fig. 3E). As calculated from EPR spectra, a Lorentzian line, with  $g$  factor of 2.0032 similar to that of free charge (2.0023) [45] assigned to the unpaired charges for the C atoms in the heptazine units, could be delocalized across the conjugated  $\pi$ - $\pi$  system under dark and visible light condition ( $\lambda > 400 \text{ nm}$ ). Particularly, when under visible light irradiation, CNNS and the heterojunctions demonstrated an enhanced EPR signal intensity compared with those EPR under dark, which suggested the photo-induced charges were more pronounced under visible light. More importantly, the EPR signal intensity enhancement of all heterojunctions were more significant than that of CNNS ascribed to the charge and hole carriers transfer between Pdots and CNNS [64,65]. Noteworthily, as observed from Fig. 3E, PIFDTBT Pdots/CNNS heterojunction showed obviously EPR signal enhancement than that of F8DTBT Pdots/CNNS under light irradiation. It is known that carriers separation and transfer is related to the energy level difference of heterojunction and carriers mobility of semiconductor [66]. Due to the relatively significant CB and VB position difference of the heterojunction and fast hole mobility of PIFDTBT, the charge-hole carriers separation and transfer in PIFDTBT Pdots/CNNS was enhanced compared to that of F8DTBT Pdots/CNNS, thus leading to obvious EPR signal enhancement. Additionally, the electrochemical

impedance spectroscopy (EIS) also supported the charge-hole carriers transfer improvement for PIFDTBT Pdots/CNNS (Fig. 3F). The equivalent circuit with the fitted parameters showed the resistance of CNNS, PIFDTBT and PIFDTBT Pdots/CNNS were 160, 130 and 55 k $\Omega$  respectively, which suggested that superior photogenerated electrons separation and transfer from PIFDTBT Pdots to CNNS ascribed to the relatively suitable band position difference and fast hole carriers mobility [67]. As a comparison, the equivalent circuit with the fitted parameters showed the resistance of CNNS, F8DTBT and F8DTBT Pdots/CNNS were 160, 266 and 125 k $\Omega$  (Fig.S12), respectively. The non-significant resistance decrease of F8DTBT Pdots/CNNS compared to that of CNNS suggested that extremely insufficient photogenerated electrons separation and transfer between F8DTBT Pdots and CNNS due to the relatively unsuitable band position difference and slow hole carriers mobility of F8DTBT.

To further confirm the charge transfer within the heterojunctions, XPS was utilized to detect the valence states of different elements (Fig.S13A-B). The N 1s peaks of CNNS located at 398.8, 399.7 and 401.1 eV were attributed to N atoms in the form of C-N=C, N-(C)<sub>3</sub> and C-NH, respectively [22]. The S 2p binding energy peaks of PIFDTBT were resolved into S 2p3/2 (164.0, 165.6 eV) and S 2p1/2 (165.2 and 166.7 eV) [45]. It could be observed that the N 1s and S 2p of PIFDTBT Pdots/CNNS heterojunction were respectively shifted to lower and higher binding energy than those of CNNS and PIFDTBT, suggesting the existence of intermolecular  $\pi$ - $\pi$  interaction between PIFDTBT Pdots and CNNS [68]. In contrast, no obvious N 1s and S 2p XPS binding energy shifts were detected for F8DTBT Pdots/CNNS heterojunction ascribed to the weak driving force of photogenerated electrons transfer (Fig.S13C-D). The surface photovoltage spectra (SPV) also supported charge separation and transfer between PIFDTBT and CNNS. The PIFDTBT Pdots/CNNS demonstrated obviously higher photovoltage than that of CNNS (Fig.S14). It suggested the enhanced charge separation and transfer from the CB of PIFDTBT Pdots to that of the CNNS. Particularly, PIFDTBT Pdots/CNNS suggested significantly improved SPV response when the wavelength range was 400–600 nm, which was very beneficial for photocatalysis because the visible light energy mainly dominates the whole sunlight energy distribution. Therefore, it could be concluded that the XPS, EPR, EIS and SPV analyses supported that the more significant energy level difference of the PIFDTBT Pdots/CNNS heterojunction and faster carriers mobility of PIFDTBT lead to more efficient interfacial charge-hole pairs transfer than that of F8DTBT Pdots/CNNS heterojunction.

In addition, CNNS exhibited characteristic XRD peaks of 13.3° and 27.4° attributed to the (100) and (002) planes [22], respectively, while PIFDTBT and F8DTBT demonstrated amorphous structures as shown in Fig.S15. All of the Pdots/CNNS heterojunctions with different mass ratios maintained the same layered structures with respect to CNNS.

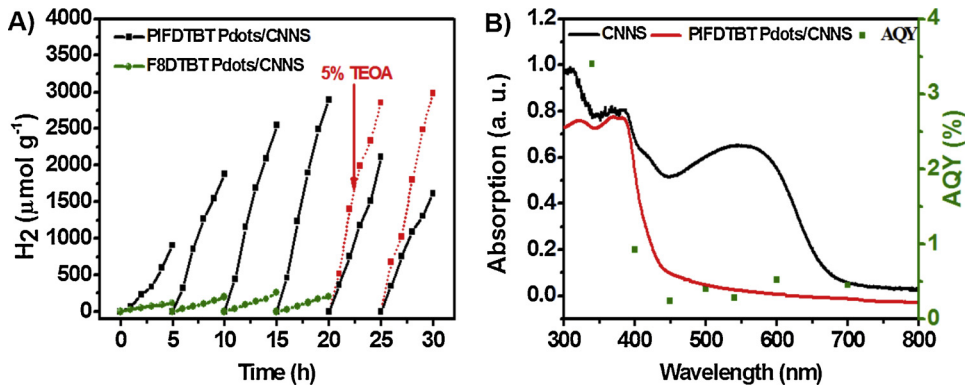
### 3.3. The improved HER of PIFDTBT Pdots/CNNS heterojunction

The photocatalytic HER experiments of CNNS, pristine conjugated polymers and the heterojunctions without co-catalysts were conducted under visible light irradiation ( $\lambda > 400$  nm) employing triethanolamine (TEOA) as a radical scavenger (Fig. 4A). No HER could be detected for either CNNS or pristine conjugated polymers. The non-detectable HER for g-C<sub>3</sub>N<sub>4</sub> was due to the fast recombination of photo-induced charges and holes, while that for the pristine conjugated polymers was ascribed to the hydrophobic characteristics of pristine conjugated polymers that led to the poor dispersion under aqueous condition and ultimately poor performance in HER. However, the average HER of PIFDTBT Pdots/CNNS and F8DTBT Pdots/CNNS heterojunctions (Pdot/CNNS = 5 wt%) was 181.1 and 23.7  $\mu\text{mol h}^{-1} \text{g}^{-1}$  at the 1<sup>st</sup> run, respectively (Fig. 4A). It meant the HER of PIFDTBT Pdots/CNNS was 7.6 times higher than that of F8DTBT Pdots/CNNS at the 1<sup>st</sup> run. The higher HER of PIFDTBT Pdots/CNNS could be also supported by the photocurrent measurements (Fig.S17). As shown in Fig.S17,

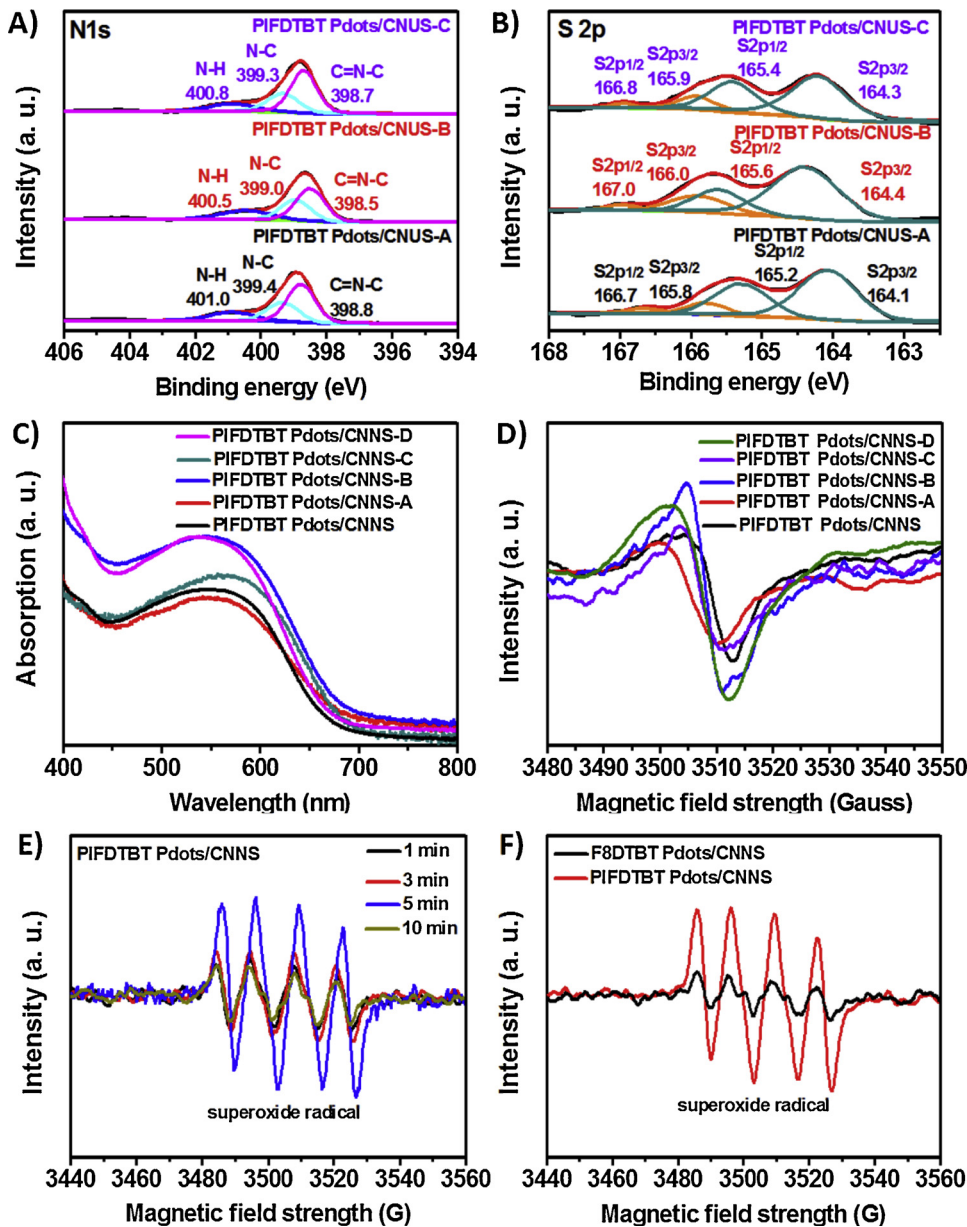
PIFDTBT Pdots/CNNS and F8DTBT Pdots/CNNS heterojunctions demonstrated higher photocurrent than those of CNNS, PIFDTBT and F8DTBT, which could be owed to the electron-hole pairs separation and transfer of the heterojunctions. Obviously, PIFDTBT Pdots/CNNS had significantly higher photocurrent than that of F8DTBT Pdots/CNNS, which suggested the more efficient photogenerated electron-hole carriers separation and transfer efficiency of PIFDTBT Pdots than that of F8DTBT Pdots due to the more suitable band position difference and faster carriers mobility, thus leading to higher HER. Meanwhile, the positive effect of Pdots on HER could be proved by 4.1 times higher HER of PIFDTBT Pdots/CNNS than that of PIFDTBT/CNS (Fig.S16A), with only 2.1 times larger specific surface area of PIFDTBT Pdots/CNNS than that of PIFDTBT/CNS (Table S1). In addition, it was found that the HER was positively correlated with the increasing PIFDTBT ratio from 1.0 to 5.0 wt% (Fig.S16B). The increase of PIFDTBT/CNNS weight ratio could lead to the enhancement in light absorption and acceleration in the separation and transfer of charge-hole pairs, resulting in the improved HER. However, the further increased PIFDTBT ratio of 7 wt% led to regional PIFDTBT aggregation on CNNS, therefore it could not significantly improve the absorption of visible light and the transfer of charge-hole pairs, resulting in limited HER increase [69].

To investigate the photocatalytic stability, the HER cycling measurements were conducted over PIFDTBT Pdots/CNNS-5% and F8DTBT Pdots/CNNS under visible light irradiation ( $> 400$  nm). Interestingly, as observed from Fig. 4A, the average HER of PIFDTBT Pdots/CNNS significantly increased from 181.1  $\mu\text{mol h}^{-1} \text{g}^{-1}$  at the 1<sup>st</sup> run to 578.1  $\mu\text{mol h}^{-1} \text{g}^{-1}$  at the 4<sup>th</sup> run, but obviously decreased to 321.8  $\mu\text{mol h}^{-1} \text{g}^{-1}$  at the 5<sup>th</sup> run. The calculated maximum AQY was 3.4% at 420 nm at the 4<sup>th</sup> run (Fig. 4B). As a comparison, the average HER of F8DTBT Pdots/CNNS only increased from 23.7  $\mu\text{mol h}^{-1} \text{g}^{-1}$  at the 1<sup>st</sup> run to 51.9  $\mu\text{mol h}^{-1} \text{g}^{-1}$  at the 3<sup>rd</sup> run, and then decreased to 40.3  $\mu\text{mol h}^{-1} \text{g}^{-1}$  at the 4<sup>th</sup> run, which suggested the HER enhancement of PIFDTBT Pdots/CNNS increased from 7.6 at the 1<sup>st</sup> run to 14.3 times at the 4<sup>th</sup> run compared to F8DTBT Pdots/CNNS, respectively. And obviously, PIFDTBT Pdots/CNNS also suggested improved photocatalysis stability because it demonstrated 1 run delay of HER decrease compared to that of F8DTBT Pdots/CNNS, which could be probably ascribed to the enhanced rigid structure of PIFDTBT. To investigate the HER regularity over different runs, XPS, EPR and UV-vis DRS were employed to detect the structure and optical change at different photocatalysis runs.

For the recovered PIFDTBT Pdots/CNNS-B (Fig. 5A), which was irradiated for 3 runs with 10 vol% TEOA, the N 1s XPS demonstrated a decrease of binding energy compared with that of the fresh PIFDTBT Pdots/CNNS (Fig.S13A). While for the recovered PIFDTBT Pdots/CNNS-C, which was irradiated for 6 runs with 10% TEOA, exhibited an increase of N 1s XPS binding energy compared with that of the recovered PIFDTBT Pdots/CNNS-B (Fig. 5A). Correspondingly, the S 2p binding energy of the recovered PIFDTBT Pdots/CNNS-B increased compared with that of fresh PIFDTBT Pdots/CNNS, while the S 2p binding energy for the recovered PIFDTBT Pdots/CNNS-C decreased compared with that of PIFDTBT Pdots/CNNS-B (Fig. 5B, Fig.S13B). Therefore, it could be seen that the intermolecular interaction of PIFDTBT Pdots/CNNS could be enhanced under light irradiation at the first 3 runs [68], while the interaction could be weakened under further light irradiation. The surface analysis by XPS (Table S5) and elemental analysis (Table S6) further supported the assumption as well. The S atomic ratios determined by XPS for the fresh PIFDTBT Pdots/CNNS was 0.73%, while that for the fresh PIFDTBT Pdots/CNNS, recovered PIFDTBT Pdots/CNNS-B and PIFDTBT Pdots/CNNS-C after being washed by chloroform for 3 times were 0.05%, 0.37% and 0.20%, respectively, and the corresponding O atomic ratios increasingly reached 2.33%, 3.07% and 4.78%, respectively. The increase of S and O atoms ratios in PIFDTBT Pdots/CNNS-B (when compared with the washed fresh PIFDTBT Pdots/CNNS) might evidence the possible chemical bonding between PIFDTBT Pdots and CNNS by oxygen-containing



groups (Table S5), while the further increase of O atom ratios in the washed PIFDTBT Pdots/CNNS-C (when compared with the washed PIFDTBT Pdots/CNNS-B) can probably prove the possible decomposition of PIFDTBT Pdots by oxygen-containing radicals (Table S5 and Table S6).



Moreover, as shown in Fig.S18A, the FT-IR of PIFDTBT Pdots/CNNS after light irradiation showed a red shift of C-H stretching assigned to  $-\text{CH}_2-$  of alkyl groups in PIFDTBT compared with PIFDTBT Pdots/CNNS before irradiation. Specifically, the characteristic peak of  $-\text{CH}_2-$  groups was red-shifted from 2925 cm<sup>-1</sup> (PIFDTBT Pdots/CNNS) to

Fig. 5. A) N1s XPS spectra of recovered PIFDTBT Pdots/CNNS-A without TEOA after visible light irradiation for 3 runs, recovered PIFDTBT Pdots/CNNS-B with 10 vol% TEOA after visible light irradiation for 3 runs and recovered PIFDTBT Pdots/CNNS-C with 10 vol % TEOA after visible light irradiation for 6 runs. B) S 2p XPS spectra of recovered PIFDTBT Pdots/CNNS-A, recovered PIFDTBT Pdots/CNNS-B and recovered PIFDTBT Pdots/CNNS-C. (The recovered PIFDTBT Pdots/CNNS heterojunctions were washed by chloroform for 3 times before XPS characterization) C) UV-vis DRS of PIFDTBT Pdots/CNNS-A, PIFDTBT Pdots/CNNS-B, PIFDTBT Pdots/CNNS-C, PIFDTBT Pdots/CNNS-D (PIFDTBT Pdots/CNNS-D was irradiation for 6 runs with 5 vol% TEOA re-addition after the 4<sup>th</sup> run). D) EPR spectra of PIFDTBT Pdots/CNNS-A, PIFDTBT Pdots/CNNS-B, PIFDTBT Pdots/CNNS-C and PIFDTBT Pdots/CNNS-D. E) DMPO spin-trapping ESR spectra for DMPO-O<sub>2</sub><sup>•-</sup> over different visible light irradiation time recorded with PIFDTBT Pdots/CNNS. F) DMPO spin-trapping ESR spectra for DMPO-O<sub>2</sub><sup>•-</sup> produced by PIFDTBT Pdots/CNNS and F8DTBT Pdots/CNNS with visible light irradiation time of 5 min. All of the ESR tests were carried out with methanol as the solvent. The mass ratio of PIFDTBT Pdots to CNNS was 5 wt% before photocatalysis.

2922 cm<sup>-1</sup> (PIFDTBT Pdots/CNNS-B, PIFDTBT Pdots/CNNS-C). It has been reported that superoxide radical ·O<sub>2</sub><sup>-</sup> could react with the α-hydrogen and α-proton of P3HT [70]. Therefore, probably the ·O<sub>2</sub><sup>-</sup> generated from the reduction of O<sub>2</sub> by PIFDTBT Pdots/CNNS under light irradiation could oxidize the α-hydrogen and α-proton of alkyl groups in PIFDTBT, which could give rise to the red shift of –CH<sub>2</sub> of alkyl groups in PIFDTBT.

Furthermore, both UV-vis DRS (Fig. 5C) and EPR (Fig. 5D) intensities for the recovered PIFDTBT Pdots/CNNS-B demonstrated pronounced increase compared with those of the fresh PIFDTBT Pdots/CNNS, while the recovered PIFDTBT Pdots/CNNS-C showed UV-vis DRS and EPR intensities decrease for the recovered PIFDTBT Pdots/CNNS-C. Obviously, due to the energy level difference, the photo-induced hole carriers of CNNS transferred to the VB of PIFDTBT Pdots, which could be further captured by TEOA. Simultaneously, it has been also proved that the porous ultrathin g-C<sub>3</sub>N<sub>4</sub> nanosheets can generate O<sub>2</sub><sup>•-</sup> and OH<sup>•</sup> under light and air conditions [56]. The E<sub>0</sub> (O<sub>2</sub>/O<sub>2</sub><sup>•-</sup>) and E<sub>0</sub> (OH/OH<sup>•</sup>) was -0.046 eV and 2.38 eV vs NHE [56], respectively, therefore the CB of CNNS was negative enough to reduce O<sub>2</sub> to O<sub>2</sub><sup>•-</sup>, while the VB of CNNS were not positive enough to oxidize OH to OH<sup>•</sup>. And despite the system was degassed prior to photocatalysis, some slight air residue and dissolved oxygen in water still existed in the system, which could lead to the formation of O<sub>2</sub><sup>•-</sup> during photocatalysis. To identify the formation of O<sub>2</sub><sup>•-</sup> produced by the heterojunctions, the ESR spectra, using DMPO as the radical spin-trapping probe for O<sub>2</sub><sup>•-</sup>, were obtained as shown in Fig. 5E-F. The obvious ESR signals suggested that the electrons in the CB of PIFDTBT Pdots/CNNS was negative enough to reduce O<sub>2</sub> to produce O<sub>2</sub><sup>•-</sup> (Fig. 5E). And the ESR intensity increased with the irradiation time increasing in the range of 1–5 min, which could be owed to increased concentration of DMPO-O<sub>2</sub><sup>•-</sup>. While the ESR intensity decreased significantly after 10 min irradiation, which could be due to the annihilation of DMPO-O<sub>2</sub><sup>•-</sup> after a certain of time (Fig. 5E). As a comparison, the ESR intensity of DMPO-O<sub>2</sub><sup>•-</sup> produced by PIFDTBT Pdots/CNNS was much weaker than that produced by PIFDTBT Pdots/CNNS under the same conditions (Fig. 5F). It could be speculated that PIFDTBT possessed more negative CB than that of F8DTBT (Fig. 3B), therefore, the CB of CNNS in PIFDTBT Pdots/CNNS was more negative than of CNNS in F8DTBT Pdots/CNNS after the photo-induced electrons transfer between Pdots and CNNS, leading to more production of O<sub>2</sub><sup>•-</sup> by PIFDTBT Pdots/CNNS. As the strong oxidizing property, O<sub>2</sub><sup>•-</sup> could react with PIFDTBT to form PIFDTBT· [70], which might produce chemical bonding with CNNS. Therefore, the recovered PIFDTBT Pdots/CNNS demonstrated increased O atomic ratios proved by XPS elemental analyses. The initial slight chemical bonding could probably accelerate carriers transfer between PIFDTBT Pdots and CNNS, therefore enhancing the light absorption and HER. However, with the irradiation time increasing, the effective conjugated chain length of PIFDTBT Pdots might be reduced as the decomposition by O<sub>2</sub><sup>•-</sup>, leading to the light absorption and HER decrease.

To further prove the active specie of ·O<sub>2</sub><sup>-</sup>, EPR analysis for PIFDTBT Pdots/CNNS were conducted under air condition as shown in Fig.S18B. The EPR intensity of PIFDTBT Pdots/CNNS significantly increased after

an irradiation time of 5 min compared with the fresh PIFDTBT Pdots/CNNS, which could be owed to the enhanced intermolecular interaction resulted from a chemical bonding between PIFDTBT Pdots and CNNS by ·O<sub>2</sub><sup>-</sup> [71]. Therefore, it could be confirmed that the reduction of O<sub>2</sub> could produce an active specie of ·O<sub>2</sub><sup>-</sup> that could enhance electron transfer between PIFDTBT and CNNS.

To further confirm the possibility of decomposition for PIFDTBT Pdots, PIFDTBT Pdots/CNNS heterojunction was under visible light irradiation for 3 runs without TEOA under the same conditions (PIFDTBT Pdots/CNNS-A). It could be seen the recovered PIFDTBT Pdots/CNNS-A showed increase in the binding energies of N 1s XPS and decrease in the binding energies of S 2p XPS (Fig. 5A-B) compared with PIFDTBT Pdots/CNNS-C. Simultaneously, the intensities of UV-vis DRS and EPR for PIFDTBT Pdots/CNNS-A significantly decreased compared to those of PIFDTBT Pdots/CNNS-C (Fig. 5C-D). Moreover, the decomposition of PIFDTBT Pdots could be clearly observed from TEM images. It could be seen that the PIFDTBT Pdots appeared obscure under light irradiation without TEOA (Fig. 5A), which should be ascribed to the Pdots decomposition, while PIFDTBT Pdots maintained clear appearance under light irradiation with TEOA as radical scavenger (Fig. 5B-C). Therefore, the XPS, FT-IR, UV-vis DRS, EPR and TEM could identify that PIFDTBT Pdots could decompose under a certain period of light irradiation, which reduced the interfacial light absorption and carriers transfer, ultimately leading to the HER decrease.

Interestingly, a re-addition of TEOA could effectively enhance the stability of HER. The HER could gradually reach 570.8 and 596.0 μmol h<sup>-1</sup> g<sup>-1</sup> at the 5<sup>th</sup> and 6<sup>th</sup> runs respectively with a re-addition of 5 vol% TEOA after the 4<sup>th</sup> run (Fig. 4A). As shown in Fig. 5C-D, PIFDTBT Pdots/CNNS-D, which was irradiated for 6 runs with a re-addition of 5 vol% TEOA after the 4<sup>th</sup> run, showed obvious enhancement in the intensities of UV-vis DRS and EPR compared with those of PIFDTBT Pdots/CNNS-C. The enhancement should be ascribed to the promoted capture of holes and oxygen-containing radicals by TEOA during photocatalysis that reduced the decomposition of PIFDTBT, resulting in the HER recovery (Fig. 6).

### 3.4. The HER mechanism of PIFDTBT Pdots/CNNS heterojunction

Based on the above results and analyses, it could be deduced that the introduction of electron-donating units into PIF could promote the light absorption efficiency, adjust the band positions, improve the carriers mobility and enhance the stability, therefore effectively improve the intermolecular π-π interaction of the PIFDTBT Pdots/CNNS heterojunction, leading to enhanced photocatalytic HER efficiency.

Herein, the structure engineering strategy of conjugated polymer structure for the heterojunctions formed between Pdots and g-C<sub>3</sub>N<sub>4</sub> was illustrated in Fig. 7. When electron-donating indenofluorene units were introduced into the backbone, the carriers separation and transfer of PIFDTBT could be accelerated under light irradiation. As the energy level difference of PIFDTBT Pdots/CNNS and fast hole carriers mobility, the photo-induced charge-hole pairs recombination could be suppressed. Due to the higher VB energy level of g-C<sub>3</sub>N<sub>4</sub>, the photo-induced

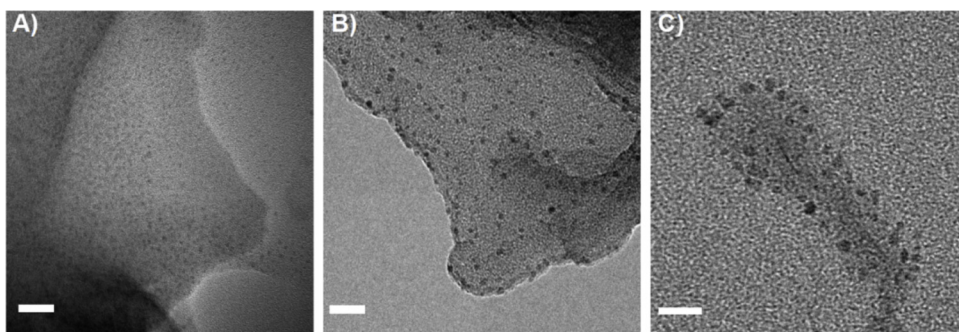


**Fig. 6.** TEM of PIFDTBT Pdots/CNNS-A (A), PIFDTBT Pdots/CNNS-B (B), and PIFDTBT Pdots/CNNS-D (C) (scale bars for all TEM images: 20 nm, the recovered PIFDTBT Pdots/CNNS heterojunctions were not washed by chloroform before TEM characterization). The mass ratio of PIFDTBT Pdots to CNNS was 5 wt % before photocatalysis.

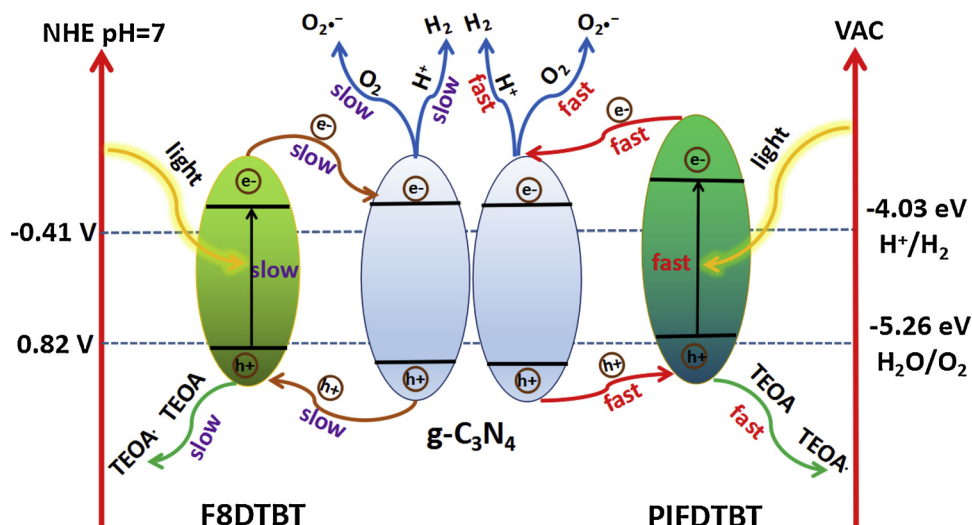


**Fig. 7.** Proposed photocatalytic mechanism of PIFDTBT Pdots/CNNS heterojunction.

MNT\_ELSEVIER\_JOURNAL\_SNB\_126948\_110

hole carriers in CNNS could transfer to the VB of PIFDTBT Pdots, and then be directly captured by TEOA. Simultaneously, the slight O<sub>2</sub><sup>•-</sup> residue in the system could be reduced by photo-induced charges in CNNS to form O<sub>2</sub><sup>•-</sup> during the photocatalysis. As the strong oxidizing property, a part of O<sub>2</sub><sup>•-</sup> could react with PIFDTBT to generate PIFDTBT<sup>\*</sup>, which might further produce chemical bonding with CNNS. The slight chemical bonding could probably accelerate carriers transfer between PIFDTBT Pdots and CNNS, which enhanced the light absorption and HER. However, with the irradiation time increased, PIFDTBT Pdots could be partly decomposed that reduced the effective conjugated chain length, leading to decreased light absorption and HER. Moreover, ascribed to the fast hole carriers mobility which could accelerate the combination of holes and TEOA, the photo-induced charges transfer from PIFDTBT Pdots to the CB of g-C<sub>3</sub>N<sub>4</sub> could be accordingly promoted, thus resulting in significant HER enhancement. In contrast, as the relatively poor light absorption, insignificant CB difference of F8DTBT Pdots/CNNS and slow hole carriers mobility of F8DTBT, the photo-induced carriers transfer between F8DTBT Pdots and g-C<sub>3</sub>N<sub>4</sub> could be constrained. The relatively insufficient photo-induced electron transfer from the CB of F8DTBT to the CB of CNNS resulted in slow production of O<sub>2</sub><sup>•-</sup> by F8DTBT Pdots/CNNS compared with that of PIFDTBT Pdots/CNNS. Accordingly, the EPR and PL suggested PIFDTBT Pdots/CNNS had much more significant photogenerated electrons transfer efficiency from the CB of PIFDTBT to the CB of g-C<sub>3</sub>N<sub>4</sub> than those of F8DTBT Pdots/CNNS, thus leading to significant HER enhancement of PIFDTBT Pdots/CNNS compared to that of F8DTBT Pdots/CNNS.

#### 4. Conclusions

In summary, a donor-acceptor (D-A) type PIF (PIFDTBT) was proved to possess light absorption capability and fast hole carriers mobility compared to corresponding D-A type PF (F8DTBT). As the relatively significant CB and VB position difference of the heterojunction, fast hole carriers mobility, improved light-harvesting capability and rigid donor structure of PIFDTBT, the PIFDTBT Pdots/CNNS demonstrated significantly improved intermolecular photogenerated electrons transfer, enhanced HER and improved photocatalysis stability compared to F8DTBT Pdots/CNNS. Under light irradiation, the interfacial interaction of the PIFDTBT Pdots/CNNS was further enhanced that significantly led to accelerated carriers transfer, promoted light

absorption and improved HER. However, the PIFDTBT Pdots could be decomposed under further irradiation, resulting in the decrease of light absorption and HER. While a re-addition of TEOA after a certain irradiation time could effectively inhibit the Pdots decomposition, thus leading to improved HER stability. In addition to visible light absorption, carriers mobility adjustments and photocatalytic stability for water splitting, this study provided a structure engineering strategy by electron donor alteration and a stability enhancement approach for conjugated polymer-based nanoconposites in the applications of photocatalysis and optical devices.

#### Declaration of Competing Interest

The authors declare that they have no known competing financial interests or personal relationships that could have appeared to influence the work reported in this paper.

#### Acknowledgements

The authors thank the National Natural Science Foundation of China (Grant No. 51833011) and the Guangdong Yang Fan Innovative & Entrepreneurial Research Team Program (Project No. 201633002).

#### Appendix A. Supplementary data

Supplementary material related to this article can be found, in the online version, at doi:<https://doi.org/10.1016/j.apcatb.2019.118067>.

#### References

- [1] T. Hisatomi, J. Kubota, K. Domen, Chem. Soc. Rev. 43 (2014) 7520–7535.
- [2] C. Acevedo, M.L. Miguel, J. Stone, R. Schmidt, J.G. Thomas, Q. Ding, H. Chang, Nat. Mater. 14 (2015) 1245–1251.
- [3] G. Zhou, Y. Shan, Y. Hu, X. Xu, L. Long, J. Zhang, J. Dai, J. Guo, J. Shen, S. Li, L. Liu, X. Wu, Nat. Comm. 9 (2018) 3366.
- [4] Y. Zheng, L. Lin, B. Wang, X.C. Wang, Angew. Chem. Int. Ed. 54 (2015) 12868–12884.
- [5] X. Wang, K. Maeda, A. Thomas, K. Takanabe, G. Xin, J.M. Carlsson, K. Domen, M. Antonietti, Nat. Mater. 8 (2009) 76–80.
- [6] A. Vinu, K. Ariga, T. Mori, T. Nakanishi, S. Hishita, D. Golberg, Y. Bando, Adv. Mater. 17 (2005) 1648–1652.
- [7] G. Zhang, Q.H. Ji, Z. Wu, G.H. Wang, H.J. Liu, J.H. Qu, J.H. Li, Adv. Funct. Mater. 28 (2018) 1706462.
- [8] S.W. Cao, J.X. Low, J.G. Yu, M. Jaroniec, Adv. Mater. 27 (2015) 2150–2176.

[9] J. Xu, M. Fujitsuka, S. Kim, Z.P. Wang, T. Majimaa, *Appl. Catal. B: Environ.* 241 (2019) 141–148.

[10] J. Xu, Z.P. Wang, Y.F. Zhu, *ACS Appl. Mater. Interfaces* 9 (2017) 27727–27735.

[11] D.M. Chen, K.W. Wang, W.Z. Hong, R.L. Zong, W.Q. Yao, Y.F. Zhu, *Appl. Catal. B: Environ.* 166 (2015) 366–373.

[12] X.Q. Fan, L.X. Zhang, R.L. Cheng, M. Wang, M.L. Li, Y.J. Zhou, J.L. Shi, *ACS Catal.* 5 (2015) 5008–5015.

[13] Q. Hao, S.M. Hao, X.X. Niu, X. Li, D.M. Chen, H. Ding, *Chin. J. Catal.* 38 (2017) 278–286.

[14] X. Dong, F. Cheng, *J. Mater. Chem. A Mater. Energy Sustain.* 3 (2015) 23642–23652.

[15] G.G. Zhang, Z.A. Lan, L.H. Lin, S. Lin, X.C. Wang, *Chem. Sci.* 7 (2016) 3062–3066.

[16] L.M. Song, T.T. Li, S.J. Zhang, *J. Phys. Chem. C.* 121 (2017) 293–299.

[17] X. Chen, Q. Liu, Q.L. Wu, P.W. Du, J. Zhu, S.Y. Dai, S.F. Yang, *Adv. Funct. Mater.* 26 (2016) 1851–1851.

[18] X. Bai, L. Wang, R. Zong, Y. Zhu, *J. Phys. Chem. C.* 117 (2013) 9952–9961.

[19] X.H. Li, X.C. Wang, M. Antonietti, *Chem. Sci.* 3 (2012) 2170–2174.

[20] L.X. Wang, F. Zhao, Q. Han, C.G. Hu, L.X. Lv, N. Chen, L.T. Qu, *Nanoscale.* 7 (2015) 9694–9702.

[21] M.L. Li, L.X. Zhang, X.Q. Fan, M.Y. Wu, M. Wang, R.L. Cheng, L.L. Zhang, H.L. Yao, J.L. Shi, *Appl. Catal. B: Environ.* 201 (2017) 629–635.

[22] P.J. Yang, H.H. Ou, Y.X. Fang, X.C. Wang, *Angew. Chem. Int. Ed.* 56 (2017) 3992–3996.

[23] Y.F. Li, R.X. Jin, X. Yan, J.Q. Li, S.Y. Song, X.C. Liu, M. Li, R.C. Jin, *Adv. Ener. Mater.* 6 (2016) 1601273.

[24] Y.F. Guo, J. Li, Y.P. Yuan, L. Li, M.Y. Zhang, C.Y. Zhou, Z.Q. Lin, *Angew. Chem. Int. Ed.* 55 (2016) 14693–14697.

[25] L. Sun, M.J. Yang, J. Huang, D.S. Yu, W. Hong, X.D. Chen, *Adv. Funct. Mater.* 26 (2016) 4943–4950.

[26] S.C. Yan, Z.S. Li, Z.G. Zou, *Langmuir.* 26 (2010) 3894–3901.

[27] N. Sagara, S. Kamimura, T. Tsubota, T. Ohno, *Appl. Catal. B: Environ.* 192 (2016) 193–198.

[28] Y. Zhang, T. Mori, J. Ye, M. Antonietti, *Chem.-Asian J.* 132 (2010) 6294–6295.

[29] Y.P. Zhu, T.Z. Ren, Z.Y. Yuan, *ACS Appl. Mater. Inter.* 7 (2015) 16850–16856.

[30] K.N. Ding, L.L. Wen, M.Y. Huang, Y.F. Zhang, Y.P. Lu, Z.F. Chen, *Phys. Chem. Chem. Phys.* 18 (2016) 19217.

[31] L. Gang, N. Ping, C.H. Sun, S.C. Smith, Z.G. Chen, Q.G. Lu, H.M. Cheng, *J. Am. Chem. Soc.* 132 (2010) 11642–11648.

[32] M.H. Vu, M. Sakar, C.C. Nguyen, T.O. Do, *ACS Sustain. Chem. Eng.* 6 (2018) 4194–4203.

[33] J.Y. Qin, J.P. Huo, P.Y. Zhang, J. Zeng, T.T. Wang, H.P. Zeng, *Nanoscale.* 8 (2016) 2249–2259.

[34] W.R. Cheng, H. Su, F.M. Tang, W. Che, Y.Y. Huang, X.H. Zheng, T. Yao, J.K. Liu, F.C. Hu, Y. Jiang, Q.H. Liu, S.Q. Wei, *J. Mater. Chem. A Mater. Energy Sustain.* 5 (2017) 19649.

[35] Y.G. Li, R.R. Wang, H.J. Li, X.L. Wei, J. Feng, K.Q. Liu, Y.Q. Dang, A.N. Zhou, *J. Phys. Chem. C.* 119 (2015) 20283–20292.

[36] J.L. Yuan, J.Q. Wen, Y.M. Zhong, X. Li, Y.P. Fang, S.S. Zhang, W. Liu, *J. Mater. Chem. A Mater. Energy Sustain.* 3 (2015) 18244–18255.

[37] S. Kumar, N. Reddy, A. Kumara, M. Shankar, V. Krishnan, *Int. J. Hydrogen Energ.* 43 (2018) 3988–4002.

[38] Q. Han, B. Wang, J. Gao, L.T. Qu, *Angew. Chem. Int. Ed.* 55 (2016) 10849–10853.

[39] J. Liu, Y. Liu, N.Y. Liu, Y.Z. Han, X. Zhang, H. Huang, Y. Lifshitz, S.T. Lee, J. Zhong, Z.H. Kang, *Science.* 347 (2015) 970–974.

[40] A. Suryawanshi, P. Dhanasekaran, D. Mhamane, S. Kelkar, S. Patil, N.M. Gupta, S. Ogale, *Int. J. Hydrogen Energ.* 37 (2012) 9584–9589.

[41] J.S. Zhang, M.W. Zhang, R.Q. Sun, X.C. Wang, *Angew. Chem. Int. Ed.* 51 (2012) 10145–10149.

[42] Y. Sui, J.H. Liu, Y.W. Zhang, X. Tian, W. Chen, *Nanoscale.* 5 (2013) 9150–9155.

[43] H.J. Yan, Y. Huang, *Chem. Commun.* 47 (2011) 4168–4170.

[44] F.T. Yu, Z.Q. Wang, S.C. Zhang, H.N. Ye, K.Y. Kong, X.Q. Gong, J.L. Hua, H. Tian, *Adv. Funct. Mater.* 28 (2018) 1804512.

[45] J. Chen, C.L. Dong, D.M. Zhao, Y.C. Huang, X.X. Wang, L. Samad, L.N. Dang, M. Shearer, S.H. Shen, L.J. Guo, *Adv. Mater.* 29 (2017) 1606198.

[46] J.L. Li, T.Y. Liu, Y.C. Chen, *Acc. Chem. Res.* 45 (2012) 1491–1500.

[47] P.J. Tseng, C.L. Chang, Y.H. Chan, L.Y. Ting, P.Y. Chen, C.H. Liao, M.L. Tsai, H. Chou, *ACS Catal.* 8 (2018) 7766–7772.

[48] Y.J. Cheng, S.H. Yang, C.H. Hsu, *Chem. Rev.* 109 (2009) 5868.

[49] M. Svensson, F. Zhang, S.C. Veenstra, W.J.H. Verhees, J.C. Hummelen, J.M. Kroon, O. Inganäs, M.R. Andersson, *Adv. Mater.* 15 (2003) 988.

[50] Y. Gao, Y.F. Deng, H.K. Tian, J.D. Zhang, D.H. Yan, Y.H. Geng, F.S. Wang, *Adv. Mater.* 29 (2017) 1606217.

[51] L. Gao, Z.G. Zhang, L.W. Xue, J. Min, J.Q. Zhang, Z.X. Wei, Y.F. Li, *Adv. Mater.* 28 (2016) 1884–1890.

[52] L. Wang, R. Fernandezteran, L. Zhang, D.L. Fernandes, L. Tian, H. Chen, H. Tian, *Angew. Chem. Int. Ed.* 55 (2016) 12306–12310.

[53] W. Zhou, T. Jia, H.X. Shi, D.S. Yu, W. Hong, X.D. Chen, *J. Mater. Chem. A Mater. Energy Sustain.* 7 (2019) 303–311.

[54] H. Kim, N. Schulte, G. Zhou, Klaus Müllen, F. Laquai, *Adv. Mater.* 23 (2011) 894.

[55] Q. Zheng, B.J. Jung, J. Sun, H.E. Katz, *J. Am. Chem. Soc.* 132 (2010) 5394–5404.

[56] J. Dia, J.X. Xia, X.W. Li, M.X. Ji, H. Xua, Z.G. Chen, H.M. Li, *Carbon.* 107 (2016) 1–10.

[57] S.H. Zang, G.G. Zhang, P.J. Yang, D.D. Zheng, X.C. Wang, *Chem. Eur. J.* 25 (2019) 1–7.

[58] J.C. Jia, N.N. Zheng, Z.F. Wang, Y.P. Huang, C.H. Duan, F. Huang, Y. Cao, *Sci. China Chem.* 60 (2017) 1458–1467.

[59] Q. Hou, Y.S. Xu, W. Yang, M. Yuan, J.B.P.Y. Cao, *J. Mater. Chem.* 12 (2002) 2887–2892.

[60] R. Street, K. Song, J. Northrup, S. Cowan, *Phys. Rev. B.* 83 (2011) 616–619.

[61] S. Lee, S. Hotta, F. Nakanishi, *J. Phys. Chem. A* 104 (2000) 1827–1833.

[62] M.Y. Ye, Z.H. Zhao, Z.F. Hu, L.Q. Liu, H.M. Ji, Z.R. Shen, T.Y. Ma, *Angew. Chem. Int. Ed.* 56 (2017) 1–6.

[63] Z.Y. Zhang, J.D. Huang, M.Y. Zhang, Q. Yuan, B. Dong, *Appl. Catal. B: Environ.* 163 (2015) 298–305.

[64] G.G. Zhang, M.W. Zhang, X.X. Ye, X.Q. Qiu, S. Lin, X.C. Wang, *Adv. Mater.* 26 (2014) 805.

[65] J.S. Zhang, G.G. Zhang, X.F. Chen, S. Lin, L. Mohlmann, G. Dolega, G. Lipner, M. Antonietti, S. Blechert, X.C. Wang, *Angew. Chem. Int. Ed.* 51 (2012) 3183.

[66] J.A. Mikroyannidis, A.N. Kabanakis, P. Balraju, G.D. Sharma, *Langmuir.* 26 (2010) 17739–17748.

[67] M. Ye, Z. Zhao, Z. Hu, L. Liu, H. Ji, Z. Shen, T. Ma, *Angew. Chem. Int. Ed.* 129 (2017) 8407–8411.

[68] Y. Zheng, Y. Jiao, Y. Zhu, L.H. Li, Y. Han, Y. Chen, A. Du, M. Jaroniec, S.Z. Qiao, *Nat. Commun.* 5 (2014) 3783.

[69] Z. Xing, Z.G. Chen, X. Zong, L.Z. Wang, *Chem. Commun. (Camb.)* 50 (2014) 6762.

[70] Y. Aoyama, T. Yamanari, T.N. Murakami, T. Nagamori, K. Marumoto, H. Tachikawa, *Polym. J.* 47 (2015) 26–30.

[71] Y.Y. Wang, W.J. Yang, X.J. Chen, J. Wang, Y.F. Zhu, *Appl. Catal. B: Environ.* 220 (2018) 337–347.